Research Article

Gani Purwiandono, Is Fatimah*, Imam Sahroni, Putwi Widya Citradewi, Azlan Kamari, Suresh Sagadevan, Won-Chun Oh, and Ruey-an Doong

Fe_3O_4@SiO_2 nanoflakes synthesized using biogenic silica from *Salacca zalacca* leaf ash and the mechanistic insight into adsorption and photocatalytic wet peroxidation of dye

https://doi.org/10.1515/gps-2022-0034
received December 10, 2021; accepted March 01, 2022

Abstract: Water pollution has become one of the most serious environmental issues recently, especially in relation to chemical-containing wastewater. Uncontrolled industrial waste, including large amounts of dye-containing wastewater from textile industries, needs intensive attention. In this work, the synthesis of Fe_3O_4@SiO_2 nanocomposite biogenic silica from *Salacca zalacca* leaf ash was conducted for the photo-Fenton-like degradation of dye waste. The use of *Salacca zalacca* leaf ash and the nanoflake form is the novelty of this work. The physicochemical characterization of the material was conducted using X-ray diffraction (XRD), scanning electron microscope (SEM), transmission electron microscope (TEM), and diffuse reflectance UV-visible spectroscopy (UV-DRS) analyses, and photocatalytic activity of material was investigated in wet peroxidation of rhodamine B and batik wastewater. The results showed homogeneously dispersed Fe_3O_4 in SiO_2 support with a nanoflake form, and a crystallite size of 44.9 nm was obtained. XRD investigation revealed the single phase of Fe_3O_4, which is consistent with the TEM analysis. The bandgap energy of 2.21 eV was reported from UV-DRS measurements, which influenced the increasing photocatalytic activity and reusability of the nanocomposite compared to pure Fe_3O_4. The photocatalyst showed the maximum degradation efficiency (DE) of 99.9% after 60 min, and the reusability feature was expressed, as there was an insignificant change in the DE over the fifth cycle of use. The material exhibited photocatalytic oxidation of batik wastewater as the removal of total suspended solids, chemical oxygen demand, and color reached 95.55%, 89.59%, and 90.00%, respectively.

Keywords: biogenic silica, Fe_3O_4@SiO_2, nanocomposite, dye waste, advanced oxidation process

1 Introduction

Water pollution has become one of the most serious environmental issues recently, especially in relation to chemical-containing wastewater. Uncontrolled industrial waste, including large amounts of dye-containing wastewater from textile industries, needs intensive attention [1,2]. Persistent chemicals and their toxicity in wastewater are known to cause serious negative effects on the aquatic environment and human life, such as carcinogenic and mutagenic effects [3,4]. Within the classification of dye-utilizing industries, batik is a popular traditional dying industry in Indonesia, and it reaches 50,000 small home industries. Considering that each company uses dyes and that the home industries discharge dye-containing wastewater in large amounts

---

*** Corresponding author: Is Fatimah,** Department of Chemistry, Faculty of Mathematics and Natural Sciences, Universitas Islam Indonesia, Kampus Terpadu UII, Jl. Kaliurang Km 14, Sleman, Yogyakarta, Indonesia, e-mail: isfatimah@uii.ac.id, tel: +62 274 896 439
Gani Purwiandono, Imam Sahroni, Putwi Widya Citradewi: Department of Chemistry, Faculty of Mathematics and Natural Sciences, Universitas Islam Indonesia, Kampus Terpadu UII, Jl. Kaliurang Km 14, Sleman, Yogyakarta, Indonesia
Azlan Kamari: Department of Chemistry, Faculty of Science and Technology, Universiti Pendidikan Sultan Idris, Kampus Tanjong Malim, Perak, 35900, Malaysia
Suresh Sagadevan: Nanotechnology and Catalysis Research Center (NANOCAT), Universiti Malaya, Kuala Lumpur, Malaysia
Won-Chun Oh: Department of Advanced Materials Science and Engineering, Hanseo University, Seosan-si, Chungnam 356-706, South Korea
Ruey-an Doong: Institute of Analytical and Environmental Sciences, National Tsing Hua University, 101, Sec 2, Kuang Fu Road, Hsinchu, 30013, Taiwan

during batik production, simple, economic, and efficient techniques for wastewater treatment are required for environmental and business sustainability [5].

Many techniques have been reported for the degradation of dye contaminants, such as Fenton and photo-Fenton oxidation procedures, including photocatalytic peroxidation (PCPO) [1]. These procedures have been noted to be more effective compared with adsorption or other methods due to their low cost and ease of use. Complete oxidation of organic compounds producing harmless CO_2 and H_2O is possible in these methods. The photoactive materials for these applications are mainly iron oxide-based materials, and in order to enhance their photocatalytic activity, structures supporting iron oxide within solid supports have been developed [6–8]. Within this scope, some papers have notified that Fe_3O_4 dispersed into silica gives higher stability and photocatalytic activity enhancement due to the nanostructure formation [9]. Previous investigations have reported the immobilization of an Fe_2O_3–Fe_3O_4 mixture in biogenic silica obtained from bamboo leaf ash and the immobilization of Fe_2O_3 in SiO_2 extracted from rice husk ash [10,11].

From the perspective of the development of magnetite nanostructures and the utilization of agricultural waste, this research aimed to evaluate the capability of Fe_3O_4 dispersed in biogenic silica ($Fe_3O_4@SiO_2$) obtained from snake fruit (*Salacca zalacca*) leaf ash (SLA) as a photocatalyst. Snake fruit is widely cultivated in Indonesia, and until now, its leaves have not been utilized. Previous studies have extracted silica from snake fruit and reported the high yield of silica with high specific surface area, and these inspired to create the innovation of the use of SLA as the raw material of the photocatalyst. The evolution of the physicochemical character of these materials consists of the formation of a porous structure, bandgap energy, and chemical stability, which are advantageous for such adsorption and photocatalytic applications [12].

In referring to the physicochemical performance of the extracted silica, a potential development for supporting Fe_3O_4 was conclusively obtained, and to our knowledge, it has not yet been reported. A physicochemical study of the $Fe_3O_4@SiO_2$ synthesized using SLA and a kinetics study in the photocatalytic oxidation reaction were conducted in this research. In particular, rhodamine B (RhB) was chosen based on its widespread use in many industries, including the small-scale coloring industry (the batik industry), which potentially discharges RhB into its wastewater. RhB-contaminated water and the batik industry's wastewater must be treated due to the carcinogenicity and damage imposed on the aquatic environment. Based on these backgrounds, this research aimed to study the physicochemical characterization of $Fe_3O_4@SiO_2$ synthesized using SLA and the mechanistic insight into its activity as a photocatalyst in photocatalytic wet peroxidation and adsorption of rhodamine B and contaminants in batik wastewater.

2 Materials and methods

2.1 Materials

Salacca zalacca leaves were obtained from the agro-industrial area in Sleman, Yogyakarta Province, Indonesia. Chemicals consisting of NaOH, HCl, cetyl trimethyl ammonium bromide (CTMA), $FeCl_2{\cdot}4H_2O$, and $FeCl_3{\cdot}6H_2O$ in the analytical grade were purchased from Merck-Millipore (Darmstadt, Germany).

2.2 Preparation of materials

SiO_2 twas extracted from SLA using a procedure previously published [12]. About 10 g of SLA was refluxed with a 1 M NaOH solution for 1 h. The resulting mixture was then filtered, and the filtrate was titrated with 1 M HCl until a white gel was produced and a pH of 7.4 was reached. The precipitate was then kept in a hot air oven at 80°C overnight before sintering at 500°C to obtain a dry powder.

$Fe_3O_4@SiO_2$ was prepared by the dispersion of an iron oxide precursor into a SiO_2 slurry at an Fe content set up at 15 wt%. The SiO_2 slurry was prepared by dispersing the SiO_2 powder in double-distilled water, and then, a solution of CTMA of 2% was added. The precursor solution was prepared by mixing $FeCl_2{\cdot}4H_2O$ and $FeCl_3{\cdot}6H_2O$ in an Fe(II):Fe(III) molar ratio of 1:4, followed by the addition of 0.1 M NaOH at an Fe:$^{-}$OH molar ratio of 1:1. The mixture was stirred for 4 h and then hydrothermally treated in an autoclave overnight at 150°C. The resulting sample from these steps was cooled at −2°C before being spray-dried, and the powder was then calcined at 500°C for 4 h. For comparison purposes, Fe_3O_4 nanoparticles were also prepared by a similar method but without dispersion into a SiO_2 slurry.

2.3 Characterization of materials

The XRD spectra of the materials were obtained with a Rigaku XRD instrument. A Ni-filtered Cu Kα radiation source (λ = 1.54 Å) was utilized as the radiation source, and the measurement was taken at the 2θ range from 10° to 90° at a scanning rate of $4°\cdot min^{-1}$ and a step-size increase of 0.02°. A JASCO V760 spectrophotometer was employed for diffuse reflectance UV-visible analysis (UV-DRS) and photoluminescence (PL) spectroscopy analysis. The surface morphology of the material was determined using a scanning electron microscope-energy dispersive X-ray spectrophotometer (SEM-EDX) Phenom X, and the particle form and size were identified using a TEM on JEOL JEM 2100, which was operated with an acceleration voltage of 200 kV with a resolution of 0.1 nm. Surface profiles of the materials consisting of specific surface area, pore distribution, and pore radius parameters were recorded using gas sorption analysis on a porosimeter Nova1200 (Quantachrome) with nitrogen gas. The sample outgassing was performed at 95°C for 3 h prior to the analysis.

2.4 Photocatalytic activity evaluation

The photocatalytic activity of $Fe_3O_4@SiO_2$ was examined using photocatalytic degradation (PC) and PCPO of RhB and batik wastewater. The reactions on RhB were performed in a water-jacketed batch reactor equipped with a lamp in the center of the reactor. For the PC treatment, about 500 mL of an RhB $20\ mg\cdot L^{-1}$ solution was added with 0.25 g of photocatalyst and 0.5 mL of H_2O_2 30%. Light illumination was conducted using a UV lamp (40 W, 295 nm) and a xenon lamp (40 W). The difference between photocatalysis and photocatalytic oxidation is in the addition of oxidant in photocatalytic oxidation, while the photocatalysis process is without oxidant addition. For RhB solution as the tested dye, the progress of the reaction was monitored by ultraviolet visible spectroscopy using a colorimetric analytical method. The degradation efficiency (DE) of the treatment to RhB was calculated using the following formula:

$$\mathrm{DE}(\%) = \frac{[C]_0 - [C]_t}{[C]_0} \times 100\% \qquad (1)$$

where C_0 and C_t are the parameters at the initial time and at the time t, which are the initial concentration and the concentration at the sampling time, respectively, determined using UV-visible (UV-vis) spectrophotometric analysis.

The photocatalytic activity of $Fe_3O_4@SiO_2$ for batik wastewater treatment was performed similar to the treatment of RhB, but the photocatalyst dosage was varied at 5, 10, 20, and $25\ g\cdot L^{-1}$, and the evaluation was based on decreasing the total suspended solid (TSS), chemical oxygen demand (COD), and color. The TSS assays were conducted using the gravimetric analysis method, while COD was determined by applying chromate digestion followed by spectrophotometric analysis. The color removal efficiency was determined by comparing the absorbance values of the treated solutions at 500 nm, which is the wavelength having maximum absorbance for the wastewater sample. The parameters of the batik wastewater quality are listed in Table 1.

Table 1: The parameters of batik's wastewater quality

Parameter	Value
COD ($mg\cdot L^{-1}$)	658
TSS ($mg\cdot L^{-1}$)	2,400
Color (absorbance at 500 nm)	0.987

2.5 Adsorption study

The adsorption study of $Fe_3O_4@SiO_2$ was evaluated for RhB as the control treatment, under similar conditions, but without light illumination.

3 Results and discussion

3.1 Physicochemical characterization of $Fe_3O_4@SiO_2$

XRD analysis is the most important analysis for phase identification in material synthesis; therefore, XRD analysis was performed before other characterization techniques. Figure 1 demonstrates the XRD pattern of $Fe_3O_4@SiO_2$ in comparison with those of SiO_2 and Fe_3O_4. The diffraction peaks of Fe_3O_4 appear at $2\theta \sim 30.3$, 34.9, 43.1, 53.4, and 56.2, which are matched with the crystal planes of (2 2 0), (3 1 1), (4 0 0), (4 4 2), and (5 1 1), according to JCPDS card number 00-019-0629 [13–15]. Similar reflections are found in $Fe_3O_4@SiO_2$, except for the (4 4 2) peak, indicating the dispersion of Fe_3O_4 in the silica support. By using the corresponding peaks, the crystallite size of Fe_3O_4 was calculated based on the Scherer equation:

$$d = k\lambda/(B\cos\theta) \qquad (2)$$

where d is the mean crystalline size of the nanoparticles, λ is the wavelength of the radiation (1.5406 Å), θ is the

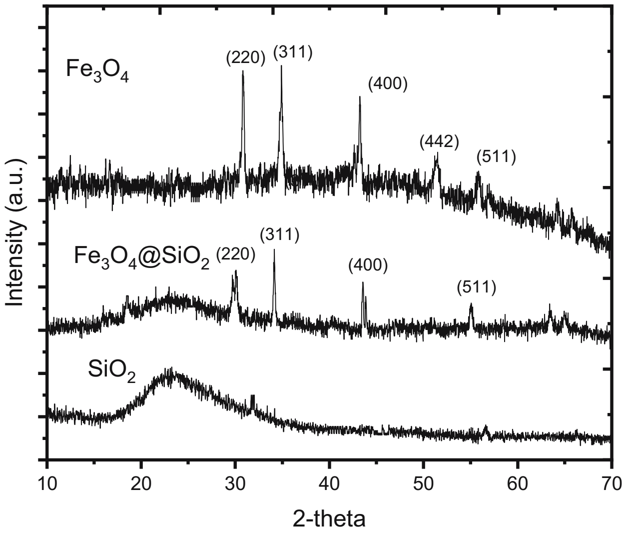

Figure 1: XRD patterns of $Fe_3O_4@SiO_2$ in comparison with Fe_3O_4 and SiO_2.

angle of the selected reflection, and *B* is the intensity of full width at half maximum (FWHM) of the selected reflection.

The calculated data are presented in Table 2, and from the calculations, it can be concluded that the mean particle size of Fe_3O_4 nanoparticles in $Fe_3O_4@SiO_2$ is 44.9 nm.

Interestingly, SEM studies (Figure 2) revealed that $Fe_3O_4@SiO_2$ composite is formed in the shape of nanoflakes. Referring to previous studies on the synthesis of Fe_3O_4, the nanoflake formation can be attributed to the formation of the goethite phase as an intermediate in the crystallite growth, in reference to the following reaction:

$$2FeOOH + Fe(OH)_2 \rightarrow Fe_3O_4 + 2H_2O \qquad (3)$$

This condition is probably facilitated by the hydrothermal condition, and in addition, the presence of support in the dispersion system contributed to generating overpressure for directing particle growth [16]. Moreover, the addition of CTMA as a template governed well-distributed nanoparticles for creating the flaky structure. This nanoflake structure also appeared for pure Fe_3O_4 as a comparison in the synthesis. A similar morphology has appeared in the preparation of Fe_3O_4 under the hydrothermal method [17] and in the dispersed Fe_3O_4 in carbon support [18]. Further EDS analyses gave the composition of the nanocomposite, as listed in Table 3. The Fe and O elements predominately existed in the $Fe_3O_4@SiO_2$ and Fe_3O_4 samples, and in particular, the Fe content was 16.9%, which is slightly higher than the set-up amount (15%).

Table 2: Calculated crystallite size from XRD measurement

2θ	**Fe_3O_4**		**$Fe_3O_4@SiO_2$**	
	FWHM	**Crystallite size**	**FWHM**	**Crystallite size**
30.3	0.143	63.8	0.128	59.8
34.9	0.145	67.6	0.149	50.0
43.1	0.227	39.9	0.179	38.8
56.2	0.158	57.2	0.235	31.3
Crystallite size (nm)	57.1		44.9	

A detailed analysis of the Fe_3O_4 nanoparticles dispersed in the SiO_2 support was performed by TEM analysis with the results presented in Figure 3. The irregular forms distributed on the silica material appeared in the $Fe_3O_4@SiO_2$ image as identified from the darker spots. Referring to the pattern, the dispersed particle sizes are within the range of 20–50 nm, which is in confirmation with the crystallite size calculated using XRD measurements mentioning the mean particle size of 44.9 nm. The range is smaller compared to the particle size distribution of pure Fe_3O_4 nanoparticles.

3.2 Optical properties of $Fe_3O_4@SiO_2$

Optical properties of $Fe_3O_4@SiO_2$ were studied using UV-DRS analysis. Figure 4 shows the UV-DRS, Tauc plot, and PL spectra of the prepared photocatalyst and Fe_3O_4. Obviously, Fe_3O_4 and $Fe_3O_4@SiO_2$ exhibit absorption in the 200–550 nm region. Moreover, $Fe_3O_4@SiO_2$ demonstrates an absorption region similar to that of Fe_3O_4. The bandgap energy values were determined using a Tauc plot with the following equation:

$$(\alpha h v)^2 = A(h v - E_g) \qquad (4)$$

where α, h, v, E_g, and A are the absorption coefficient, Planck's constant, the light frequency, the bandgap energy, and a constant, respectively. The extrapolation of the linear portion of the $(\alpha\, h\, v)^2$ curve versus hv to zero was utilized for bandgap energy estimation, and it was found that the bandgap energy of $Fe_3O_4@SiO_2$ and Fe_3O_4 materials is 2.21 and 2.19 eV, respectively. This suggests that the dispersion of magnetite into silica support slightly increases the bandgap energy. A similar pattern has also been reported from Fe_3O_4 incorporated into mesoporous silica [19–21], in that the bandgap energy is inversely proportional to the particle size. Theoretically, this increasing energy value is attributed to the decreasing particle size of the material,

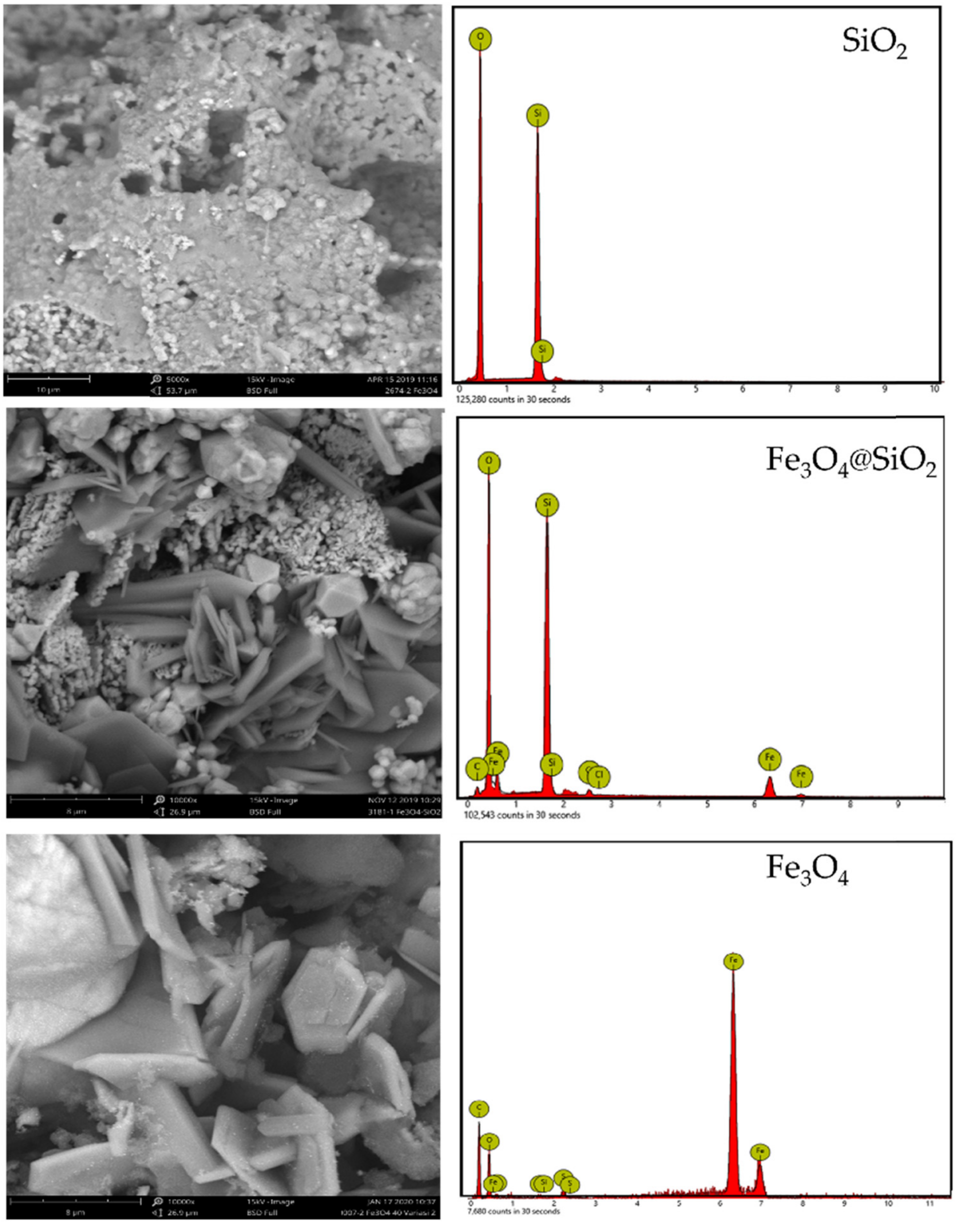

Figure 2: SEM images of $Fe_3O_4@SiO_2$, Fe_3O_4, and SiO_2.

Table 3: Elemental analysis of materials

Element	SiO_2	Fe_3O_4	$Fe_3O_4@SiO_2$
O	67.97	31.81	50.28
Si	32.03	n.d.	26.05
Fe	n.d	68.19	16.90

n.d., not detected.

which is consistent with the smaller dispersed particle size in $Fe_3O_4@SiO_2$ identified using TEM analysis. The PL spectrum in Figure 4c exhibits UV emission peaks in the range of λ = 200–400 nm and a peak in the visible region of λ = 470.50 nm. These positions correspond to the emission pattern of Fe_3O_4-containing nanocomposites in the literature [22]. The lower intensity of the peak in the visible range relative to the UV range indicates diminished electron-hole recombination [23].

Figure 5 shows the SiO_2 and $Fe_3O_4@SiO_2$ adsorption–desorption isotherms and their pore distribution profile, and the calculated parameters are presented in Table 4. Enhancement of adsorption capacity appeared, as shown by a higher adsorbed volume by $Fe_3O_4@SiO_2$ compared to pure SiO_2 at all P/P_o ranges. This is confirmed

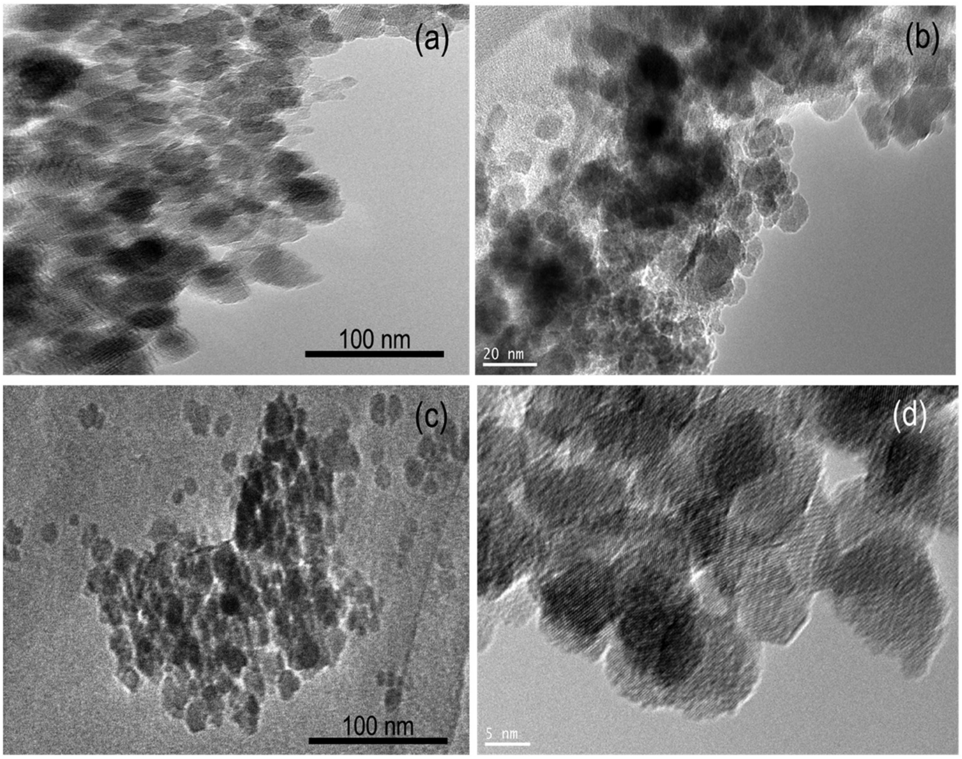

Figure 3: TEM images of (a and b) $Fe_3O_4@SiO_2$ and (c and d) Fe_3O_4 in different magnifications.

by the higher specific surface area and pore volume of $Fe_3O_4@SiO_2$, and moreover, the pore distribution reveals that the higher BET-specific surface area, external surface area, and pore volume parameters are related to the formation of modal pores at around 6.45 and 40 Å. The pore distribution suggests the change of porosity from the microporous material into the combination of microporous and mesoporous classification.

3.3 Photocatalytic activity

The comparisons of RhB removal over varied treatments – adsorption, PC, and PCPO over $Fe_3O_4@SiO_2$ – are presented by the kinetics of RhB removal in Figure 6. As expected, the removal by the photocatalytic process gave significant enhancement in RhB removal compared to the adsorption process. In more detail, the kinetics plots revealed that the photocatalytic activity of the RhB removal over PC and PCPO is higher compared to the adsorption process, in the following order: PCPO + UV > PCPO + Vis > PCPO + Vis > PC + Vis > adsorption.

Moreover, kinetics analysis of RhB removal over PC and PCPO shows that the processes obey second-order kinetics by the following equation:

$$\frac{1}{C_t} = k_{\mathrm{obs}}t + \frac{1}{C_0} \tag{5}$$

where C_t and C_0 are the concentrations of RhB at the time t and at the initial time, respectively, and k_{obs} is the observed kinetics constant [24,25]. The kinetics plots in Figure 7 show that the highest kinetics constant is observed from the PCPO process under UV and visible light over $Fe_3O_4@SiO_2$ and Fe_3O_4, and in more detail, the calculated parameters are presented in Table 5.

From the parameters presented in Table 5, it is seen that the kinetics constant and the DE of the processes utilizing $Fe_3O_4@SiO_2$ demonstrated higher activities compared to the use of Fe_3O_4 alone for all mechanisms. In addition, from the DE values, it is seen that the nearly complete removal of RhB was attained by PCPO using $Fe_3O_4@SiO_2$, which shows a higher efficiency compared to the DE achieved by Fe_3O_4 alone. This result is due to the immobilized Fe_3O_4 on the SiO_2 support. For both $Fe_3O_4@SiO_2$ and Fe_3O_4, the PCPO processes gave higher kinetics constants and DE values, suggesting the role of H_2O_2 as an oxidant in the photocatalytic system.

The presence of Fe_3O_4 as a photoactive material leads to the formation of radicals and oxidizing agents via its interaction with photons by the following mechanism [26,27]:

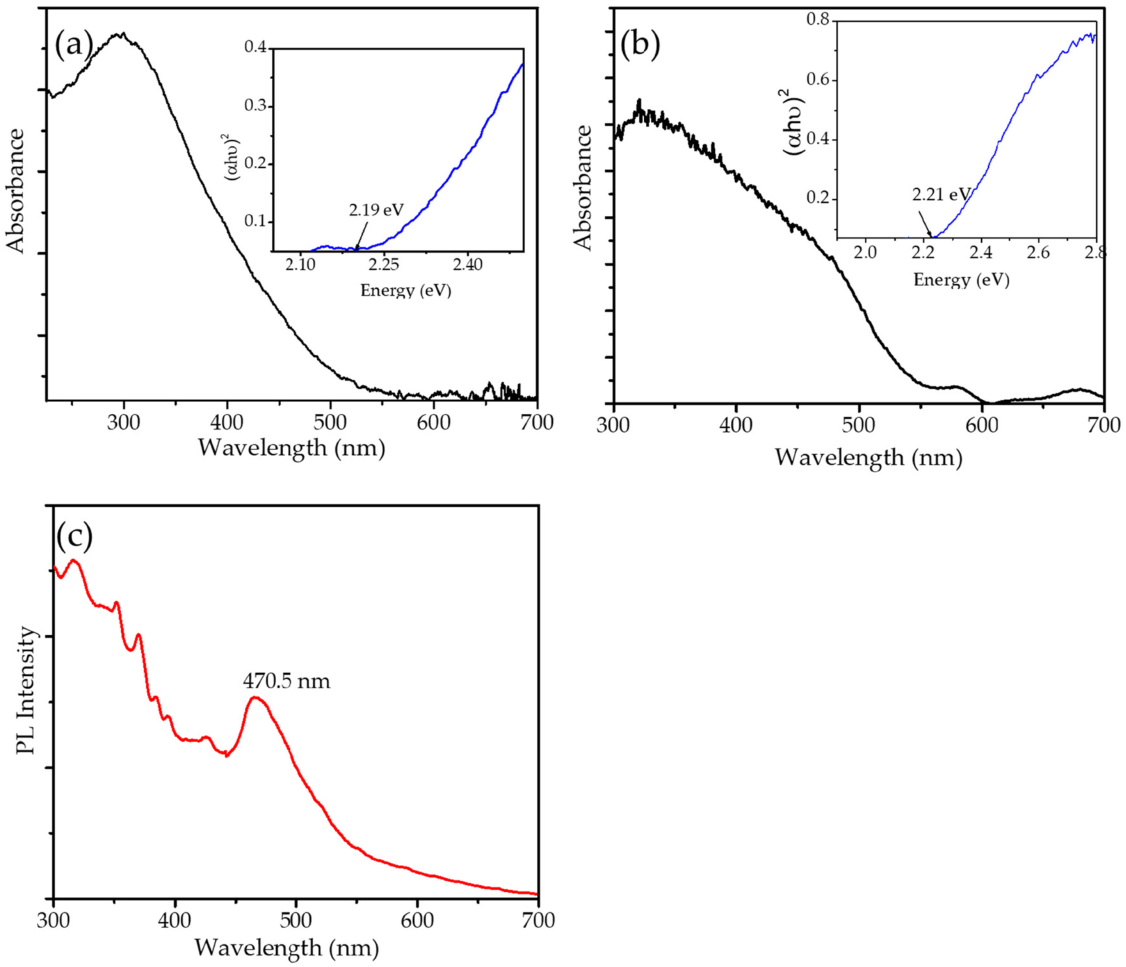

Figure 4: (a) UV-DRS spectrum of Fe_3O_4; (b) UV-DRS spectrum of $Fe_3O_4@SiO_2$; and (c) PL spectrum of $Fe_3O_4@SiO_2$.

$$Fe_3O_4 + h\nu \rightarrow Fe_3O_4 + h^+_{vb} + e^-_{cb} \tag{6}$$

$$h^+ + H_2O \rightarrow H^+ + OH^\bullet \tag{7}$$

$$h^+ + OH^- \rightarrow OH^\bullet \tag{8}$$

$$e^- + O_2 \rightarrow O_2^- \tag{9}$$

$$2e^- + O_2 + 2H^+ \rightarrow H_2O_2 \tag{10}$$

$$e^- + H_2O_2 \rightarrow OH^\bullet + OH^- \tag{11}$$

$$\text{Organic} + {}^\bullet OH + O_2 \rightarrow CO_2 + H_2O \tag{12}$$

The production of radicals is enhanced by the addition of an oxidant, producing faster propagation steps within the organic molecule degradation. The comparison between the use of UV light and visible light implied the higher feasibility of UV light exposure for accelerating the reaction mainly at the initial step of radical formation, and by the additional time of treatment, it is seen that the removal reached similar results for both PC and PCPO. Based on the DE, the photocatalytic activity of $Fe_3O_4@SiO_2$ in comparison with other materials is presented in Table 6 [28–33].

Conclusively, the photocatalytic activity of $Fe_3O_4@SiO_2$ in this work is comparable to other photocatalyst materials. The renewable resource of biogenic silica extracted from SLA becomes competitive in this degradation application.

3.4 Role of support

From the data given in Table 4, it is seen that the adsorption rate of RhB is in the following order: $Fe_3O_4@SiO_2 > SiO_2 > Fe_3O_4$. $Fe_3O_4@SiO_2$ represents the higher capability of the composite form to adsorb RhB.

The kinetics data were evaluated according to Lagergren's pseudo-first order, Ho and McKay's pseudo-second, and Weber and Morris's intraparticle diffusion models based on the following equations:

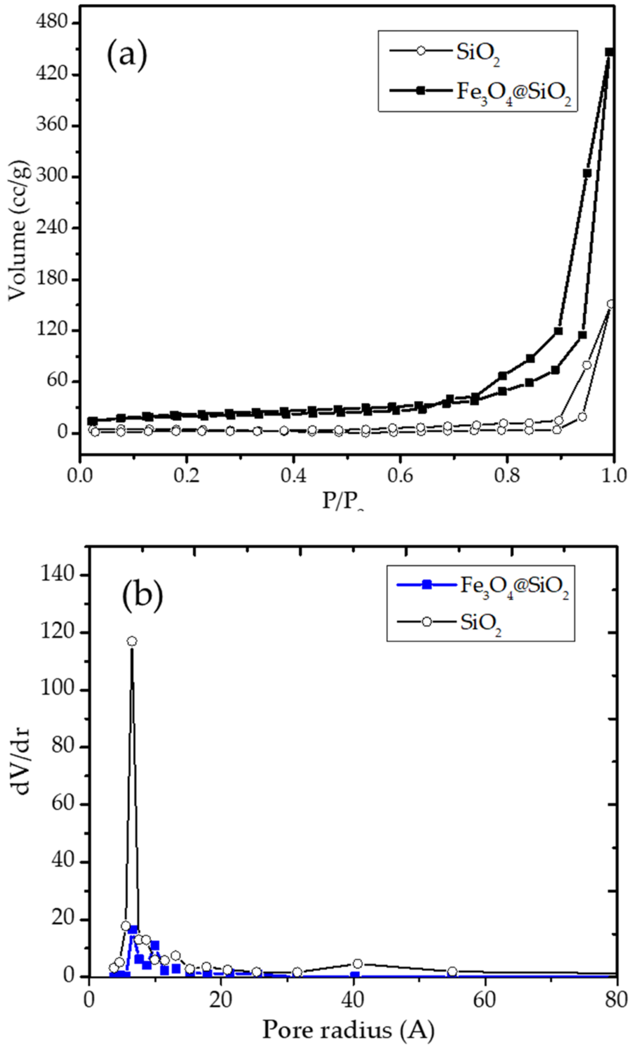

Figure 5: (a) Adsorption–desorption profile; (b) pore distribution of $Fe_3O_4@SiO_2$ in comparison with SiO_2.

Table 4: Surface parameters of $Fe_3O_4@SiO_2$ in comparison with SiO_2

Parameter	SiO_2	$Fe_3O_4@SiO_2$
BET-specific surface area ($m^2 \cdot g^{-1}$)	95.62	79.56
External surface area ($m^2 \cdot g^{-1}$)	44.69	20.84
Pore volume ($cc \cdot g^{-1}$)	0.77	0.45
Pore radius	18.29	13.34

$$\ln(q_e - q_t) = \ln q_e - k_1 t \tag{13}$$

$$\frac{t}{q_t} = \frac{1}{k_2 q_e^2} + \frac{t}{q_e} \tag{14}$$

$$q_t = k_i t^{0.5} + C \tag{15}$$

where q_e ($mg \cdot g^{-1}$) is the adsorption capacity, q_t ($mg \cdot g^{-1}$) is the amount of adsorbed metal ions at the time t, k (min^{-1}) is the first-order rate constant, k_2 [$g \cdot (mg \cdot min)^{-1}$] is the second-order rate constant of adsorption (min^{-1}), and k_i ($mg \cdot min^{1/2} \cdot g^{-1}$) and C are constants, the kinetics constant and the constant of the intra-particle diffusion model, respectively [34,35].

The kinetic parameters are listed in Table 7. Referring to the R^2 values, the adsorption by all samples represents the best fit with the intra-particle diffusion model, and the plots from these kinetics calculations are presented in Figure 8.

The fitness of the kinetics data with the pseudo-first-order kinetics suggests that the adsorption by $Fe_3O_4@SiO_2$ is largely controlled by the internal diffusion of the molecules, and so, this is the rate-controlling step during the adsorption process. The diffusion itself is influenced by the surface area, pore structure, and reactivity of the surface. In general, the small particle sizes of the adsorbent lead to

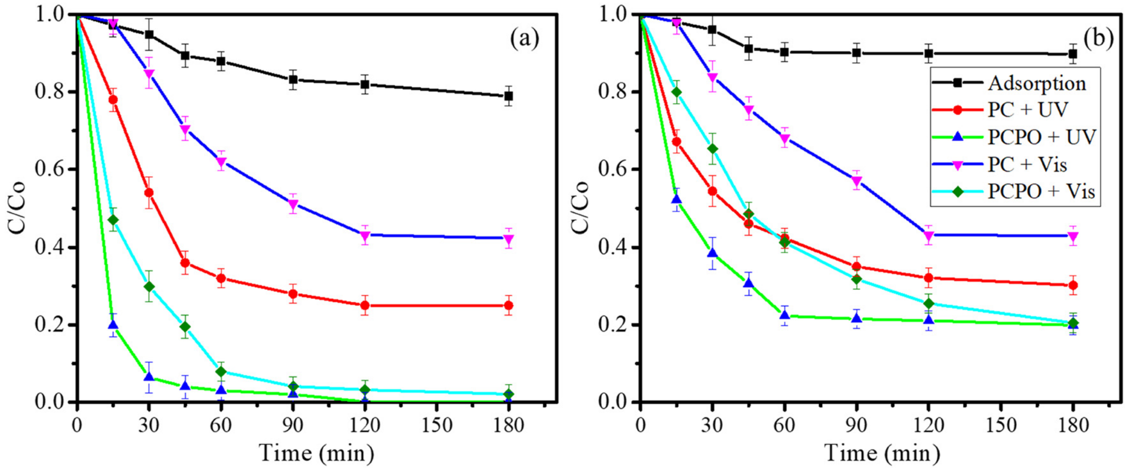

Figure 6: Kinetics plot of RhB removal utilizing various methods on (a) $Fe_3O_4@SiO_2$ and (b) Fe_3O_4.

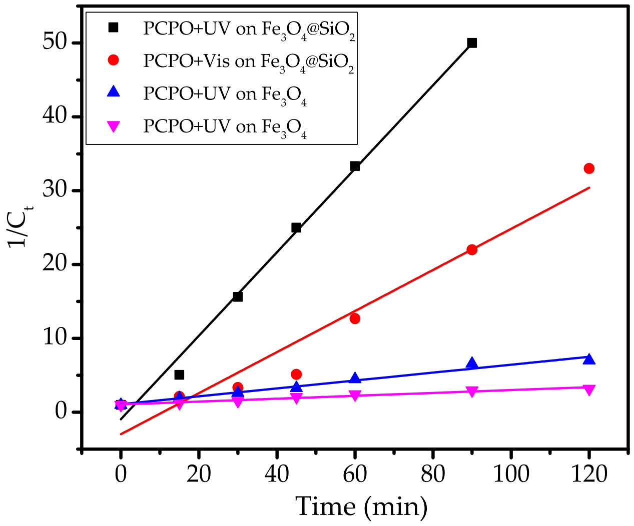

Figure 7: Second-order plots of RhB PCPO processes over $Fe_3O_4@SiO_2$ and Fe_3O_4.

the higher affinity of the adsorbate. Considering that the specific surface area of $Fe_3O_4@SiO_2$ is less than the specific surface area of SiO_2, it can be noted that the presence of the dispersed Fe_3O_4 increased the affinity by possible chemisorption. In addition, the higher adsorption capability of $Fe_3O_4@SiO_2$ compared to Fe_3O_4 alone indicates that the porous structure available in $Fe_3O_4@SiO_2$ provides the synergistic effect of both physisorption and chemisorption. This is also confirmed by the constant (intercept) values as representative of the boundary layer effect of which $Fe_3O_4@SiO_2$ has the highest value [36,37]. From this analysis, it can be concluded that photocatalysis is supported by an adsorption mechanism. The capability of Fe_3O_4 for conducting chemisorption is presented in the schematic diagram in Figure 9.

Besides the availability of pores in the composite, the adsorption of RhB occurs due to the available hydrogen bonding and electrostatic interaction among hydrophobic and hydrophilic parts [38,39]. This assumption aligns with the kinetics and adsorption model used in studies that have reported that $Fe_3O_4@C$ nanoparticles and $Fe_3O_4@SiO_2$ are functionalized by polypropylene [39].

3.5 Degradation mechanism

In order to identify the mechanism of removal, UV-Vis spectrophotometry and LCMS analyses were performed. The UV-Vis spectra of PCPO-treated solution with UV light illumination are depicted in Figure 10. The pattern suggests the evolution of the RhB spectrum along with the time of treatment has not only reduced absorbance, which serves as proof of reduced concentration, but also the redshift of the characteristic peak of 556 nm, which indicates the de-ethylation and decarboxylation of the RhB structure. These possible structural changes are confirmed by the LCMS analysis presented in Figure 11.

The comparison of the chromatograms of RhB for the initial and treated solutions showed proof of the degradation products. The presence of RhB is identified by the

Table 5: Calculated parameters from kinetics studies

Material	Process	Kinetics constant (mg·min·L^{-1})	Kinetics equation	R^2	DE (%)
$Fe_3O_4@SiO_2$	Adsorption	1.978×10^{-3}	$\frac{1}{C_t} = 1.006 \times 10^{-3}t + 1.014$	0.987	18.1
$Fe_3O_4@SiO_2$	PC + UV	2.630×10^{-2}	$\frac{1}{C_t} = 2.630 \times 10^{-2}t + 1.159$	0.973	75.9
$Fe_3O_4@SiO_2$	PCPO + UV	6.525	$\frac{1}{C_t} = 6.525t - 0.713$	0.991	99.9
$Fe_3O_4@SiO_2$	PC + Vis	0.251	$\frac{1}{C_t} = 0.251t + 0.456$	0.990	70.2
$Fe_3O_4@SiO_2$	PCPO + Vis	3.385×10^{-3}	$\frac{1}{C_t} = 3.385 \times 10^{-3}t + 0.989$	0.991	96.8
Fe_3O_4	Adsorption	9.926×10^{-4}	$\frac{1}{C_t} = 9.926 \times 10^{-4}t + 1.018$	0.987	10.1
Fe_3O_4	PC + UV	2.023×10^{-2}	$\frac{1}{C_t} = 2.023 \times 10^{-2}t + 1.053$	0.982	67.9
Fe_3O_4	PCPO + UV	3.425×10^{-2}	$\frac{1}{C_t} = 3.425 \times 10^{-2}t + 0.714$	0.989	78.5
Fe_3O_4	PC + Vis	1.018×10^{-2}	$\frac{1}{C_t} = 1.018 \times 10^{-2}t + 0.883$	0.993	56.9
Fe_3O_4	PCPO + Vis	2.228×10^{-2}	$\frac{1}{C_t} = 2.228 \times 10^{-2}t + 1.233$	0.979	68.5
SiO_2	Adsorption	1.297×10^{-3}	$\frac{1}{C_t} = 1.297 \times 10^{-4}t + 1.008$	0.978	12.8

Table 6: Photocatalytic activity of $Fe_3O_4@SiO_2$ in comparison with other materials

Material	Remark	DE (%)	Reference
$SiO_2@TiO_2$ nanospheres	Maximum DE was achieved at 4 h of treatment	~99.9	[28]
ZnO ceramic	Maximum DE was achieved at 2 h	40	[29]
$BiMnO_3$ nanoparticles	Photocatalyst dosage of 0.4 $g{\cdot}L^{-1}$, treatment for 2 h using 0.5 mL H_2O_2	90	[30]
$W(N_xS_{1-x})_2$ nanoflowers	Photocatalyst dosage of 0.2 $g{\cdot}L^{-1}$, treatment for 1 h using 0.5 mL H_2O_2 under visible light	50	[31]
Co_3O_4-Bi_2O_3	Photocatalyst dosage of 5.0 $g{\cdot}L^{-1}$, treatment for 2 h under visible light	92	[32]
α-Fe_2O_3	Maximum DE was achieved at pH 10, photocatalyst dosage of 0.8 $g{\cdot}L^{-1}$ for 40 min under UV light	90.13	[33]
Fe_2O_3/SiO_2	SiO_2 was extracted from Bamboo leaf ash, [RhB] = 20 $mg{\cdot}L^{-1}$, catalyst dosage = 0.2 g/100 mL, H_2O_2 = 1 $mL{\cdot}L^{-1}$ for 2 h	99.00	[10]
$Fe_3O_4@SiO_2$	Maximum DE was achieved at pH 7, photocatalyst dosage of 0.5 $g{\cdot}L^{-1}$ for 60 min under UV light, [RhB] = 20 $mg{\cdot}L^{-1}$, H_2O_2 = 1 $mL{\cdot}L^{-1}$	99.9	This work

Table 7: Calculated parameters from adsorption kinetics studies

Material	R^2			q_e ($mg{\cdot}g^{-1}$)
	Lagergren's pseudo-first order	Ho and McKay's pseudo-second	Weber and Morris' intraparticle diffusion	
$Fe_3O_4@SiO_2$	0.977	0.985	0.992	5.6
Fe_3O_4	0.949	0.545	0.995	4.3
SiO_2	0.990	0.245	0.995	8.6

peak at a retention time of 6.3 min. As can be seen in the treated solution, some of the other peaks appeared along with the reduced peak associated with the presence of RhB. MS analyses revealed that the fraction of *m/z* with values of 359, 331, 181, 168, 146, and 128 is identified in the spectra. These spectra elucidate the possible mechanism of degradation, which can be described by the scheme in Figure 12 [40,41].

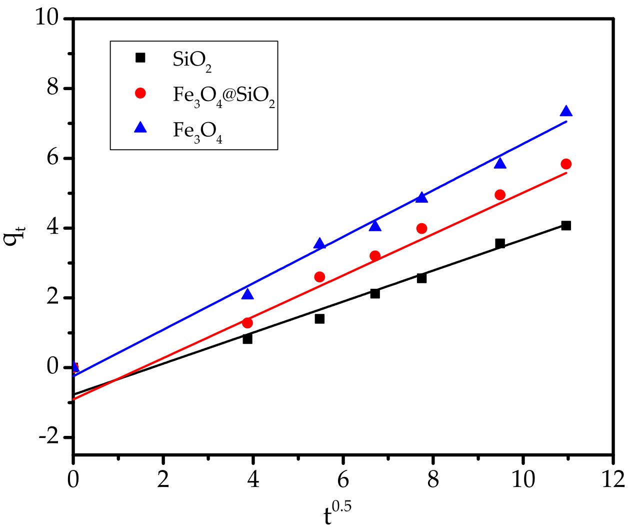

Figure 8: Intra-particle diffusion plots of RhB adsorption by $Fe_3O_4@SiO_2$, SiO_2, and Fe_3O_4.

3.6 Effect of pH

In order to examine the effect of pH, PCPO treatments using $Fe_3O_4@SiO_2$ were conducted at varied pH: 4, 7, 9, and 11. The kinetics of RhB removal at varied pH is presented in Figure 13.

The kinetics plots and initial rate data showed the optimum pH at 7, and the photodegradation rate reduced under acidic and basic conditions. The trend suggests that the surface charge properties of the photocatalyst influence the interaction between the photocatalyst surface and RhB as adsorbate. Under acidic conditions, the photocatalyst, which mainly consists of an oxide structure, will be covered with protons that have a higher affinity to the surface compared with the RhB. On the other hand, basic conditions will inhibit RhB adsorption due to the electrostatic interaction between RhB with its positive charge and the hydroxyl group. Moreover, the decomposition of H_2O_2 is retarded by the presence of OH^-, so the propagation steps occur at a slower rate [42,43]. A similar phenomenon is also presented in the photocatalytic oxidation by TiO_2 [44,45], Fe_2O_3 [44], and $Fe_3O_4@SiO_2@ZnO$ [46].

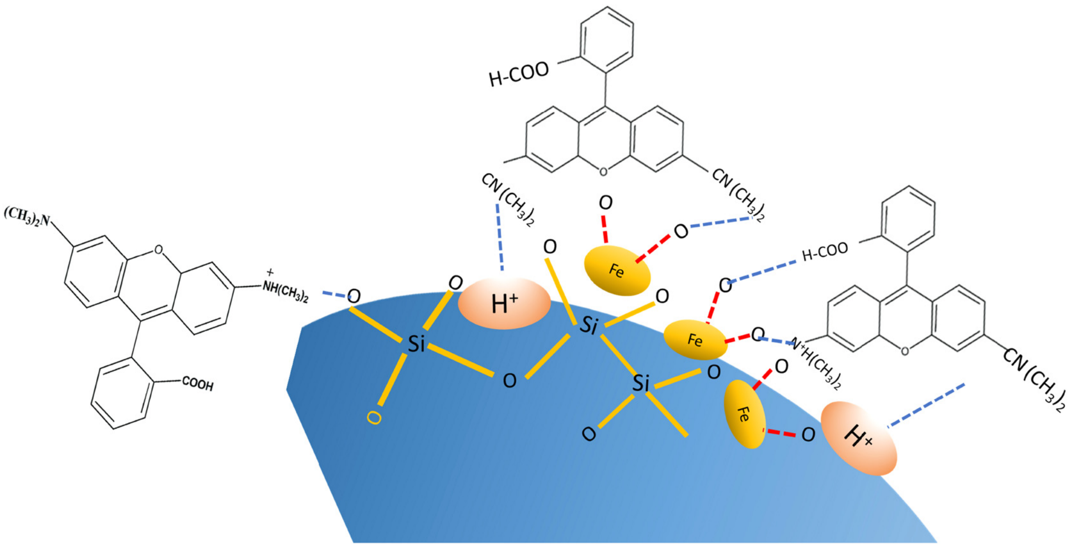

Figure 9: Schematic representation of adsorption mechanism of RhB using $Fe_3O_4@SiO_2$.

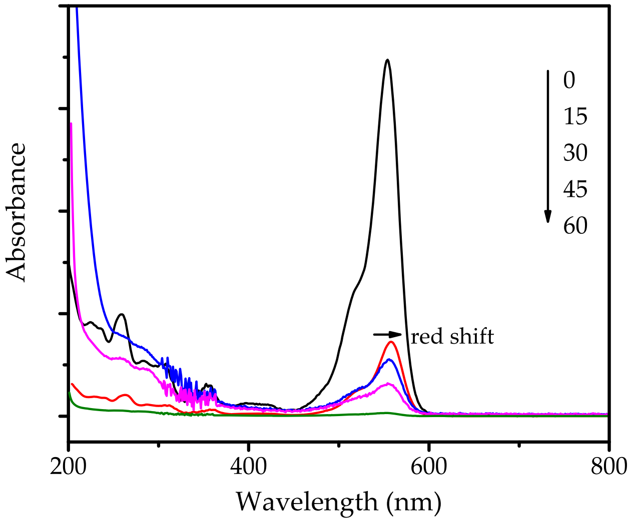

Figure 10: UV-Vis spectra of initial and treated solutions.

3.7 Effect of radical scavengers

To determine the reactive species controlling the degradation mechanism, a PCPO kinetics study with the addition of the hydroxy radical and hole to the photocatalytic system was conducted. Isopropanol (IPR) and ethylenediaminetetraacetic acid (EDTA) were employed as the hydroxy radical and hole scavenger, respectively. The kinetics plots of PCPO in the presence and absence of the scavenger are depicted in Figure 14.

It can be seen from Figure 14 that the photodegradation rate decreased with the addition of IPR and increased with the addition of EDTA. IPR in the solution has the capability of trapping the hydroxy radicals or other radical forms produced from the interaction between the holes and the solution at the initiation step. The trapping inhibited propagation steps owing to their need for further RhB oxidation. In contrast, an increasing oxidation rate was attained through the hole-blocking by EDTA, as the excited electron–hole recombination was suppressed. More electrons can migrate on the surface to further produce more radicals through interaction with the solvent or O_2. These results imply not only that the radicals were the dominant reactive species for the photocatalytic oxidation mechanism but also that the electron–hole recombination influenced the rate of reaction. A similar effect was also reported for the photocatalytic activity of Fe_2O_3 nanoparticles [47] and SnO_2 [40].

3.8 Reusability of photocatalyst

The investigation of reusability is one of the most required studies of photocatalysts for applicability on the industrial scale. The examinations were based on the DE evaluation of the fresh and recycled $Fe_3O_4@SiO_2$, which underwent five cycles. Recycling was conducted by filtering the powder, washing with ethanol, and recalcination at 200°C after the completion of each cycle. From the bar chart depicted in Figure 15, it can be seen that DE values were maintained with insignificant changes, as the DE reductions were no more than 10%. Thus, the prepared $Fe_3O_4@SiO_2$ exhibited stability, so it is noted to be potentially developed for upscaling.

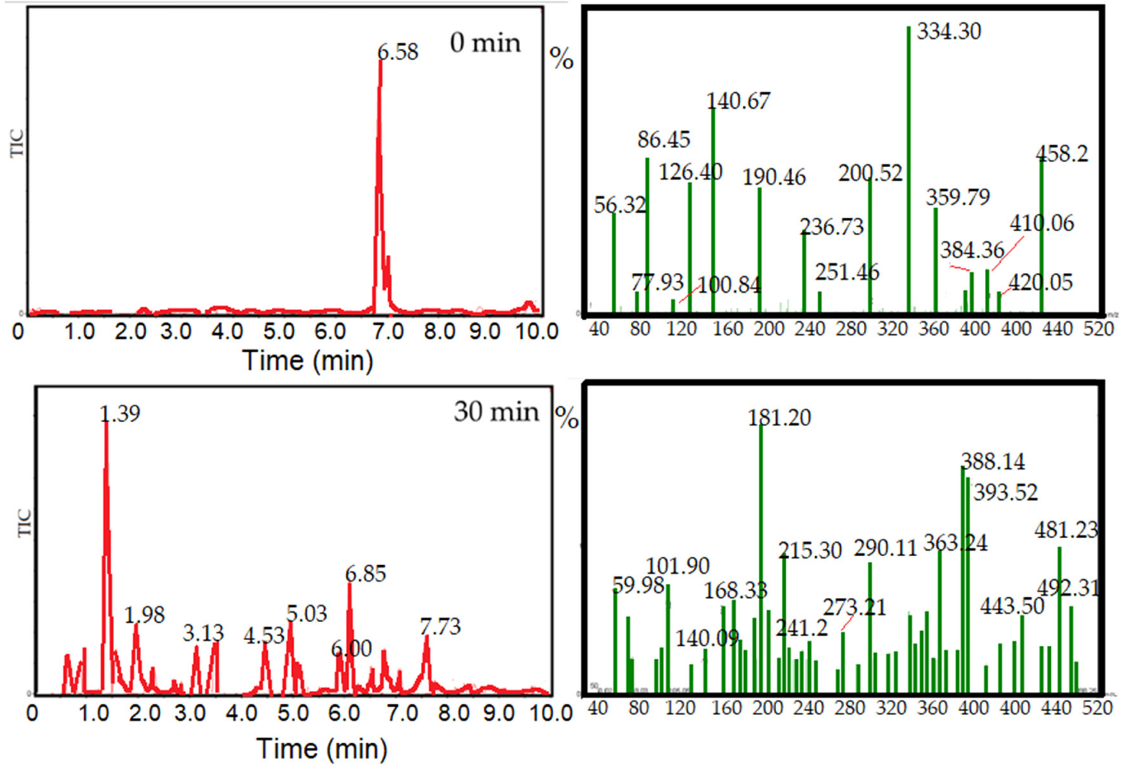

Figure 11: LCMS analysis of initial RhB and treated solution for 30 min: $[Rhb]_0 = 20\ mg{\cdot}L^{-1}$, time of treatment = 30 min, $[H_2O_2] = 1\ mL$, light = UV, and photocatalyst dose = $0.5\ g{\cdot}L^{-1}$.

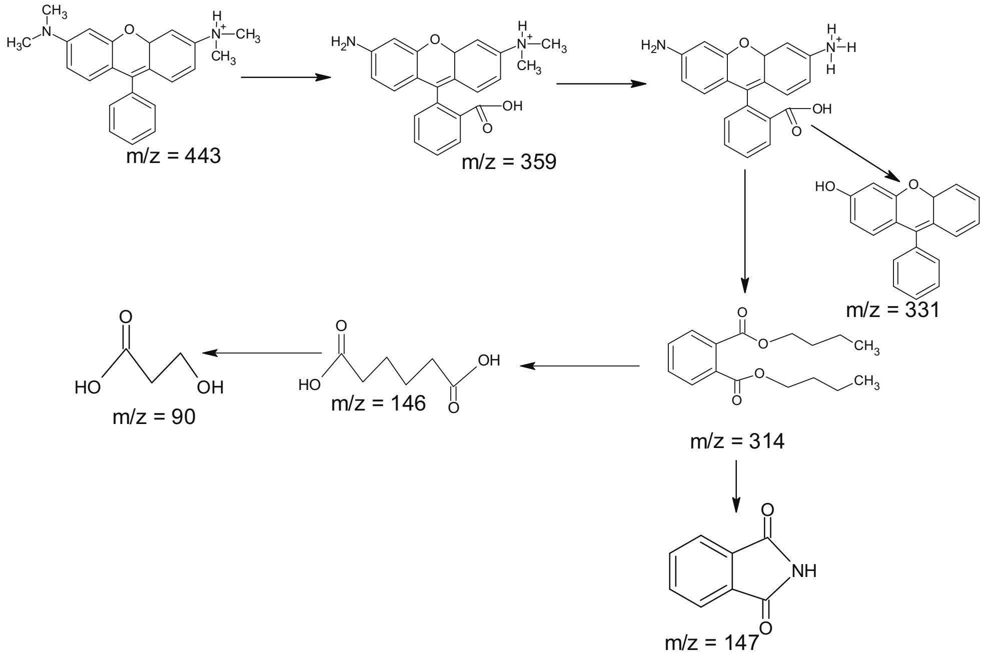

Figure 12: Possible degradation mechanism of RhB.

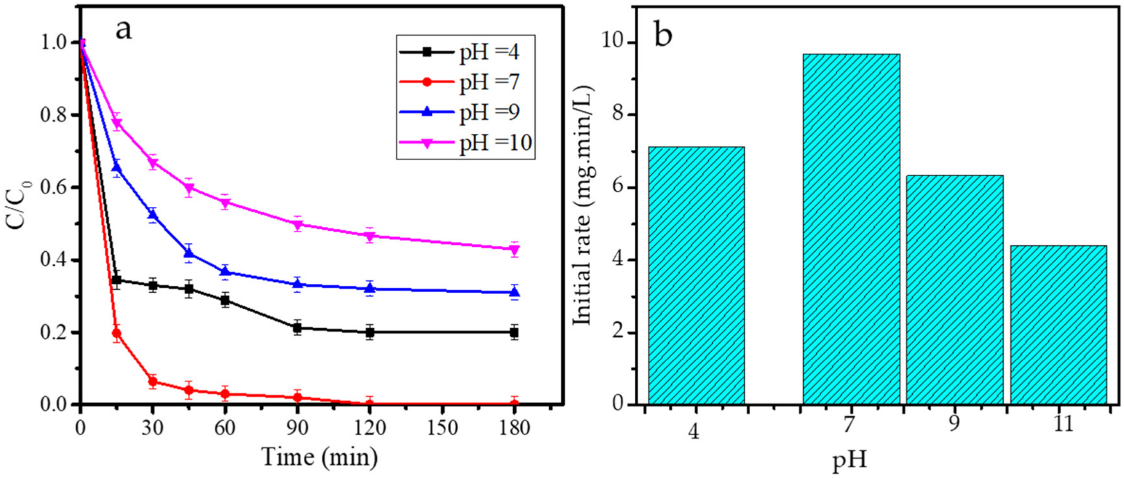

Figure 13: (a) Kinetics plots; (b) initial rate of PCPO treatments by $Fe_3O_4@SiO_2$ at varied pH.

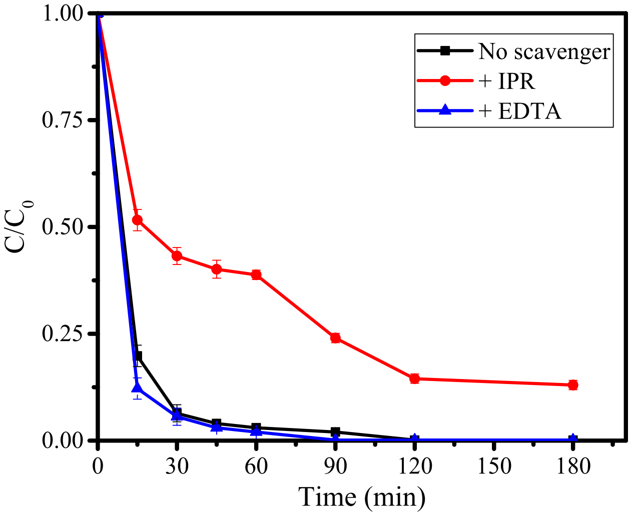

Figure 14: The kinetics of PCPO in the presence and absence of the scavengers.

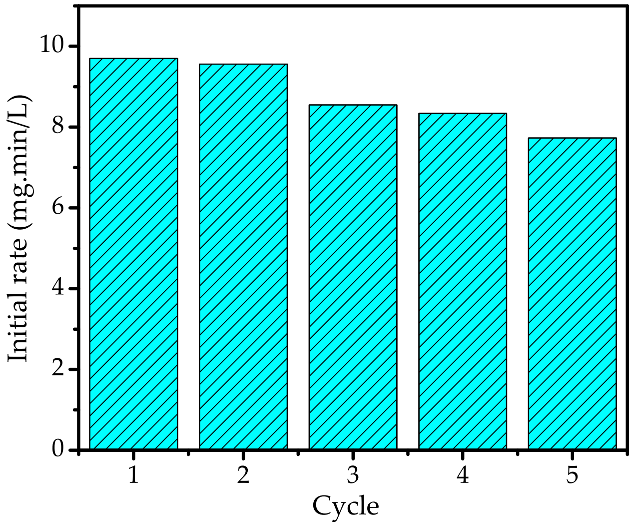

Figure 15: DE of PCPO process using $Fe_3O_4@SiO_2$ at first–fifth cycles.

Generally speaking, the prepared $Fe_3O_4@SiO_2$ exhibited excellent physicochemical properties as a photocatalyst in the PCPO process toward dye removal. As the nanocomposite is prepared by using biogenic silica extracted from SLA, the material has a high potential for being developed as a low-cost photocatalyst.

3.9 Photocatalytic activity in PCPO of batik wastewater

In order to evaluate the applicability of $Fe_3O_4@SiO_2$ for industrial wastewater, the PCPO of batik wastewater under UV light was investigated. The activity was determined based on the removal of TSS, COD, and color at varied photocatalyst doses of 5, 10, 20, and 25 $g{\cdot}L^{-1}$. The selected doses were determined by prior trials, and similar to the treatment for RhB, the treatment without light illumination was also performed. The graphs presented in Figure 16 demonstrate the effectiveness of $Fe_3O_4@SiO_2$ as a photocatalyst, as the TSS, COD, and color removals over (a) PCPO are higher compared to the adsorption process (b). It is also noted that increased removal values resulted from increased photocatalyst doses. As can be seen from the removal values, the TSS removal reached 95.55%, while the removal of COD and color is about 89.59% and 90.00%, respectively.

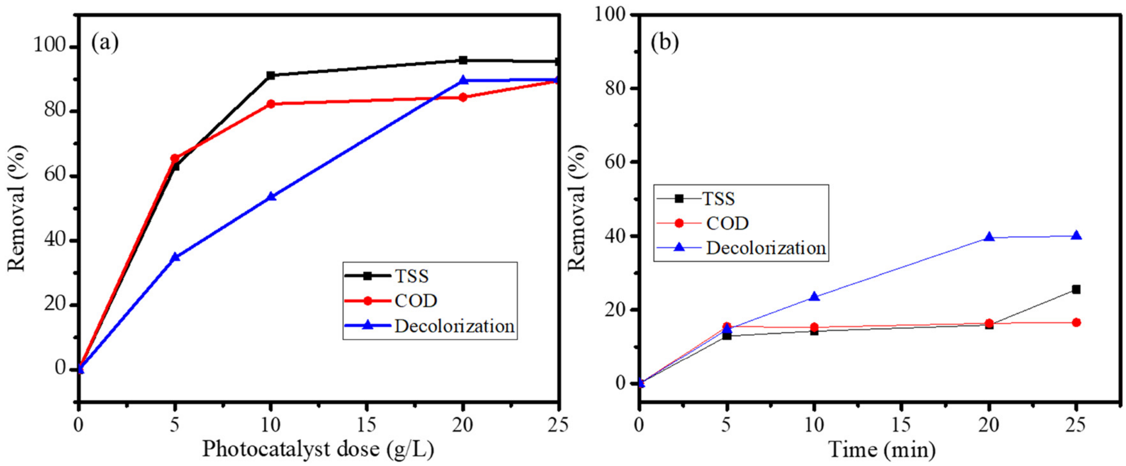

Figure 16: The removals of TSS, COD, and decolorization of Batik wastewater by (a) PCPO and (b) adsorption of $Fe_3O_4@SiO_2$.

Investigation of reusability is one of the most required studies of photocatalysts for applicability on the industrial scale. The examinations were based on the DE evaluation of the fresh and recycled $Fe_3O_4@SiO_2$, which underwent five cycles. Recycling was conducted by filtering powder, washing with ethanol, and recalcination at 200°C after the completion of each cycle. From the bar chart depicted in Figure 15, it can be seen that the DE values were maintained with insignificant changes, as the DE reductions were no more than 10%. Quantitatively, the removals are less than that of the treatment with RhB solution. In this case, batik wastewater is composed of multicomponent, being a mixture of dyes and additional preservatives in colorization. However, the effectiveness of the treatment in this work is higher compared to the photocatalytic activity of plastic-coated TiO_2 [48] and titanium dioxide (TiO_2)-coated aluminum plates [49], where the removal achieved was about 95% with the treatment for 5 days and 4 h, respectively.

Generally speaking, the finding in this work suggests the potency of SLA as the raw material of effective and low-cost photocatalyst for industrial application. Based on that, the results were obtained on a laboratory scale; of course, intensive studies on a larger scale including cost-effectiveness calculations are required.

4 Conclusion

The synthesis of $Fe_3O_4@SiO_2$ nanoflakes has been conducted by using SiO_2 derived from SLA. Physicochemical characterization of the material revealed the nanoflake form of the dispersed single-phase Fe_3O_4 onto silica support having a particle size of about 44.9 nm. Optical studies of the nanoflakes showed that the bandgap energy of 2.21 eV is higher compared to the bandgap energy of Fe_3O_4 (2.19 eV). The kinetics study of RhB removal over various methods suggested a significant increase in the photocatalytic activity of the nanoflakes compared to Fe_3O_4 in either the photocatalytic or photocatalytic oxidation processes. The highest DE was achieved by the photocatalytic oxidation process under UV light, in which about 99.9% of the RhB was removed. The support of Fe_3O_4 in SiO_2 contributed to the material reusability since it gave an insignificant change in the DE until after the fifth cycle of usage.

Acknowledgement: The authors would like to express their appreciation for the support from the Ministry of Education, Culture, Research, and Technology through the World Class Professor Program in 2021.

Funding information: Research was funded by the Ministry of Education, Culture, Research, and Technology via World Class Research 2021.

Author contributions: Gani Purwiandono: formal analysis, visualization; Is Fatimah: conceptualization, methodology; Imam Sahroni: visualization, data curation; Putwi Widya Citradewi: data curation, formal analysis; Azlan Kamari: writing – review and editing; Suresh Sagadevan: supervising, project administration; Won-Chun Oh: writing – review and editing; Ruey-an Doong: methodology, funding acquisition.

Conflict of interest: One of the authors (Suresh Sagadevan) is a member of the Editorial Board of Green Processing and Synthesis.

References

[1] Deng Y, Zhao R. Advanced oxidation processes (AOPs) in wastewater treatment. Curr Pollut Reports. 2015;1:167–76. doi: 10.1007/s40726-015-0015-z.

[2] Javaid R, Qazi UY. Catalytic oxidation process for the degradation of synthetic dyes: an overview. Int J Environ Res Public Health. 2019;16:1–27. doi: 10.3390/ijerph16112066.

[3] Gita S, Shukla SP, Saharan N, Prakash C, Deshmukhe G. Toxic effects of selected textile dyes on elemental composition, photosynthetic pigments, protein content and growth of a freshwater chlorophycean alga chlorella vulgaris. Bull Environ Contam Toxicol. 2019;102:795–801. doi: 10.1007/s00128-019-02599-w.

[4] Lellis B, Fávaro-Polonio CZ, Pamphile JA, Polonio JC. Effects of textile dyes on health and the environment and bioremediation potential of living organisms. Biotechnol Res Innov. 2019;3:275–90. doi: 10.1016/j.biori.2019.09.001.

[5] Giwa A, Yusuf A, Balogun HA, Sambudi NS, Bilad MR, Adeyemi I, et al. Recent advances in advanced oxidation processes for removal of contaminants from water: a comprehensive review. Process Saf Environ Prot. 2021;146:220–56. doi: 10.1016/j.psep.2020.08.015.

[6] Badmapriya D, Asharani IV. Dye degradation studies catalysed by green synthesized Iron oxide nanoparticles. Int J Chemtech Res. 2016;9:409–16.

[7] Meng L, Chan Y, Wang H, Dai Y, Wang X, Zou J. Recycling of iron and silicon from drinking water treatment sludge for synthesis of magnetic iron oxide@SiO_2 composites. Environ Sci Pollut Res. 2016;23:5122–33. doi: 10.1007/s11356-015-5742-6.

[8] Mehrdad A, Massoumi B, Hashemzadeh R. Kinetic study of degradation of Rhodamine B in the presence of hydrogen peroxide and some metal oxide. Chem Eng J. 2011;168:1073–8. doi: 10.1016/j.cej.2011.01.087.

[9] Pereira MC, Oliveira LCA, Murad E. Iron oxide catalysts: Fenton and Fenton-like reactions – a review. Clays Clay Miner. 2012;47:285–302.

[10] Fatimah I, Amaliah SN, Andrian MF, Handayani TP, Nurillahi R, Prakoso NI, et al. Iron oxide nanoparticles supported on biogenic silica derived from bamboo leaf ash for rhodamine B photodegradation. Sustain Chem Pharm. 2019;13:100149. doi: 10.1016/j.scp.2019.100149.

[11] Fatimah I, Fadhilah S, Mawardani SA. γ-Fe_2O_3nanoparticles immobilized in SiO_2 aerogel synthesized from rice husk ash for photofenton like degradation of rhodamine B. Rasayan J Chem. 2018;11:544–53. doi: 10.7324/RJC.2018.1122067.

[12] Fatimah I, Zaenuri FU, Doewandono LN, Yahya A, Citradewi PW, Sagadevan S. Biogenic silica extracted from salacca leaf ash for salicylic acid adsorption. Sci Technol Indones. 2021;6:296–302.

[13] Alfredo Reyes Villegas V, Isaías De León Ramírez J, Hernandez Guevara E, Perez Sicairos S, Angelica Hurtado Ayala L, Landeros Sanchez B. Synthesis and characterization of magnetite nanoparticles for photocatalysis of nitrobenzene. J Saudi Chem Soc. 2020;24:223–35. doi: 10.1016/j.jscs.2019.12.004.

[14] Sarwar A, Wang J, Khan MS, Farooq U, Riaz N, Nazir A, et al. Iron oxide (Fe_3O_4)-supported SiO_2 magnetic nanocomposites for efficient adsorption of fluoride from drinking water: synthesis, characterization, and adsorption isotherm analysis. Water (Switzerland). 2021;13. doi: 10.3390/w13111514.

[15] Zhang X, Wang G, Yang M, Luan Y, Dong W, Dang R, et al. Synthesis of a Fe_3O_4-CuO@meso-SiO_2 nanostructure as a magnetically recyclable and efficient catalyst for styrene epoxidation. Catal Sci Technol. 2014;4:3082–9. doi: 10.1039/c4cy00430b.

[16] Šutka A, Lagzdina S, Juhnevica I, Jakovlevs D, Maiorov M. Precipitation synthesis of magnetite Fe_3O4 nanoflakes. Ceram Int. 2014;40:11437–40. doi: 10.1016/j.ceramint.2014.03.140.

[17] Rudra S, Nayak AK, Koley S, Chakraborty R, Maji PK, Pradhan M. Redox-mediated shape transformation of Fe_3O_4 nanoflakes to chemically stable Au–Fe_2O_3 composite nanorods for a high-performance asymmetric solid-state supercapacitor device. ACS Sustain Chem Eng. 2019;7:724–33. doi: 10.1021/acssuschemeng.8b04300.

[18] Chen L, Xu X, Wan L, Zhu G, Li Y, Lu T, et al. Carbon-incorporated Fe_3O_4 nanoflakes: high-performance faradaic materials for hybrid capacitive deionization and supercapacitors. Mater Chem Front. 2021;5:3480–8. doi: 10.1039/d0qm00946f.

[19] Nikmah A, Taufiq A, Hidayat A. Synthesis and characterization of Fe_3O_4/SiO_2 nanocomposites. IOP Conf Ser Earth Environ Sci. 2019;276. doi: 10.1088/1755-1315/276/1/012046.

[20] Liu T, Liu L, Liu J, Liu S, Qiao SZ. Fe_3O_4 encapsulated mesoporous silica nanospheres with tunable size and large void pore. Front Chem Sci Eng. 2014;8:114–22. doi: 10.1007/s11705-014-1413-2.

[21] Hussein EA, Kareem SH. Magnetic mesoporous silica material (Fe_3O_4@mSiO_2) as adsorbent and delivery system for ciprofloxacin drug. IOP Conf Ser Mater Sci Eng. 2020;871. doi: 10.1088/1757-899X/871/1/012020.

[22] Karunakaran C, Senthilvelan S. Fe_2O_3-photocatalysis with sunlight and UV light: Oxidation of aniline. Electrochem Commun. 2006;8:95–101. doi: 10.1016/j.elecom.2005.10.034.

[23] Kurien U, Hu Z, Lee H, Dastoor AP, Ariya PA. Radiation enhanced uptake of Hg0(g) on iron (oxyhydr)oxide nanoparticles. RSC Adv. 2017;7:45010–21. doi: 10.1039/c7ra07401h.

[24] Shokoohi R, Dargahi A, Azami Gilan R, Zolghadr Nasab H, Zeynalzadeh D, Molla Mahmoudi M. Magnetic multi-walled carbon nanotube as effective adsorbent for ciprofloxacin (CIP) removal from aqueous solutions: isotherm and kinetics studies. Int J Chem React Eng. 2020;18:1–14. doi: 10.1515/ijcre-2019-0130.

[25] Samarghandi MR, Asgari G, Shokoohi R, Dargahi A, Arabkouhsar A. Removing amoxicillin antibiotic from aqueous solutions by Saccharomyces cerevisiae bioadsorbent: kinetic, thermodynamic and isotherm studies. Desalin Water Treat. 2019;152:306–15. doi: 10.5004/dwt.2019.23941.

[26] Zuorro A, Lavecchia R, Monaco MM, Iervolino G, Vaiano V. Photocatalytic degradation of azo dye reactive. Catalysts. 2019;9:645–61.

[27] Leonard K. Green synthesis of mesoporous hematite (α – Fe_2O_3) nanoparticles and their photocatalytic activity. Adv

Powder Technol. 2015;24:160–7. doi: 10.1016/j.apt.2012.04.005.

[28] Wilhelm P, Stephan D. Photodegradation of rhodamine B in aqueous solution via SiO_2@TiO_2 nano-spheres. J Photochem Photobiol A Chem. 2007;185:19–25. doi: 10.1016/j.jphotochem.2006.05.003.

[29] Ruellas TMO, Domingos GHS, Peçanha LOO, Maestrelli SC, Giraldi TR. Photodegradation of Rhodamine B catalyzed by ZnO pellets. Ceramica. 2019;65:47–53. doi: 10.1590/0366-6913201965S12609.

[30] Revathi B, Balakrishnan L, Pichaimuthu S, Nirmala Grace A, Krishna Chandar N. Photocatalytic degradation of rhodamine B using $BiMnO_3$ nanoparticles under UV and visible light irradiation. J Mater Sci Mater Electron. 2020;31:22487–97. doi: 10.1007/s10854-020-04750-4.

[31] Liu P, Zhang J, Gao D, Ye W. Efficient visible light-induced degradation of rhodamine B by W(NxS1-x)2 nanoflowers. Sci Rep. 2017;7:70784.

[32] Saeed M, Jamal MA. Co_3O_4–Bi_2O_3 heterojunction: an effective photocatalyst for photodegradation of rhodamine B dye. Arab J Chem. 2021;15(4):103732.

[33] Jahagirdar A, Ahmed Z, Donappa N, Nagabhushana H, Nagabhushana BM. Photocatalytic degradation of Rhodamine B using nanocrystalline α-Fe_2O_3. J Mater Environ Sci. 2014;5:1426–33.

[34] Zou C, Liang J, Jiang W, Guan Y, Zhang Y. Adsorption behavior of magnetic bentonite for removing Hg(II) from aqueous solutions. RSC Adv. 2018;8:27587–95. doi: 10.1039/c8ra05247f.

[35] Lee W, Yoon S, Choe JK, Lee M, Choi Y. Anionic surfactant modification of activated carbon for enhancing adsorption of ammonium ion from aqueous solution. Sci Total Environ. 2018;639:1432–9. doi: 10.1016/j.scitotenv.2018.05.250.

[36] Plazinski W, Rudzinski W. Kinetics of adsorption at solid/Solution interfaces controlled by intraparticle diffusion: a theoretical analysis. J Phys Chem C. 2009;113:12495–501. doi: 10.1021/jp902914z.

[37] Pholosi A, Naidoo EB, Ofomaja AE. Intraparticle diffusion of Cr (VI) through biomass and magnetite coated biomass: a comparative kinetic and diffusion study. South African J Chem Eng. 2020;32:39–55. doi: 10.1016/j.sajce.2020.01.005.

[38] Chatterjee S, Guha N, Krishnan S, Singh AK, Mathur P, Rai DK. Selective and recyclable congo red dye adsorption by spherical Fe_3O_4 nanoparticles functionalized with 1,2,4,5-benzenetetracarboxylic acid. Sci Rep. 2020;10:1–11. doi: 10.1038/s41598-019-57017-2.

[39] Xiang H, Ren G, Zhong Y, Xu D, Zhang Z, Wang X, et al. Fe_3O_4@C nanoparticles synthesized by in situ solid-phase method for removal of methylene blue. Nanomaterials. 2021;11:330.

[40] Fatimah I, Rubiyanto D, Sahroni I, Putra RS, Nurillahi R, Nugraha J. Physicochemical characteristics and photocatalytic performance of Tin oxide/montmorillonite nanocomposites at various Sn/montmorillonite molar to mass ratios. Appl Clay Sci. 2020;193:105671. doi: 10.1016/j.clay.2020.105671.

[41] Akbari A, Sabouri Z, Hosseini HA, Hashemzadeh A, Khatami M, Darroudi M. Effect of nickel oxide nanoparticles as a photocatalyst in dyes degradation and evaluation of effective parameters in their removal from aqueous environments. Inorg Chem Commun. 2020;115:107867. doi: 10.1016/j.inoche.2020.107867.

[42] Mahajan R, Suriyanarayanan S, Nicholls IA. Improved solvothermal synthesis of γ-Fe2O3 magnetic nanoparticles for SiO_2 coating. Nanomaterials. 2021;11. doi: 10.3390/nano11081889.

[43] Hazarika M, Saikia I, Das J, Tamuly C, Das MR. Biosynthesis of Fe_2O_3@SiO_2 nanoparticles and its photocatalytic activity. Mater Lett. 2016;164:480–3. doi: 10.1016/j.matlet.2015.11.042.

[44] Liu Y, Sun N, Hu J, Li S, Qin G. Photocatalytic degradation properties of a-Fe_2O_3 nanoparticles for dibutyl phtalate in aqueous solution system. R Soc Open Sci. 2018;5:172196.

[45] Steplin Paul Selvin S, Ganesh Kumar A, Sarala L, Rajaram R, Sathiyan A, Princy Merlin J, et al. Photocatalytic degradation of Rhodamine B using zinc oxide activated charcoal polyaniline nanocomposite and its survival assessment using aquatic animal model. ACS Sustain Chem Eng. 2018;6:258–67. doi: 10.1021/acssuschemeng.7b02335.

[46] Qin Y, Zhang H, Tong Z, Song Z, Chen N. A facile synthesis of Fe_3O_4@SiO_2@ZnO with superior photocatalytic performance of 4-nitrophenol. J Environ Chem Eng. 2017;5:2207–13. doi: 10.1016/j.jece.2017.04.036.

[47] Kusior A, Michalec K, Jelen P, Radecka M. Shaped Fe_2O_3 nanoparticles – synthesis and enhanced photocatalytic degradation towards RhB. Appl Surf Sci. 2019;476:342–52. doi: 10.1016/j.apsusc.2018.12.113.

[48] Sutisna S, Wibowo E, Rokhmat M, Rahman DY, Murniati R, Khairurrijal K, et al. Batik wastewater treatment using TiO_2 nanoparticles coated on the surface of plastic sheet. Procedia Eng. 2017;170:78–83. doi: 10.1016/j.proeng.2017.03.015.

[49] Sharfan N, Shobri A, Anindria FA, Mauricio R, Tafsili MAB, Slamet S. Treatment of batik industry waste with a combination of electrocoagulation and photocatalysis. Int J Technol. 2018;5:936–43.